


RESEARCH ARTICLE

Natural frequency prediction of the 3-RPS parallel manipulator using the substructure synthesis technology

Yaping Gong¹ and Junbin Lou² 

¹Maritime School, Zhejiang Ocean University, Zhoushan, Zhejiang, 316000, China and ²College of Information Science and Engineering, Jiaxing University, Jiaxing, Zhejiang, 314001, China

Corresponding author: Junbin Lou; Email: loujunbin1224@163.com

Received: 3 December 2022; **Revised:** 21 April 2023; **Accepted:** 28 April 2023; **First published online:** 1 June 2023

Keywords: parallel manipulator; elastodynamic; substructure synthesis; dynamic performance

Abstract

This paper proposed an elastodynamic modeling method combined with independent displacement coordinates and substructure synthesis technology. Firstly, the connecting rod was discretized, and the elastodynamic control equation for each element was established. The multipoint constraint element theory, linear algebra, and singularity analysis were used to identify the globally independent displacement coordinates of the manipulator. On this basis, the elastodynamic model using the substructure synthesis for the 3-PRS parallel manipulator (PM) was developed, with its natural frequencies distribution in the regular workspace discussed. The comparison with the finite-element results showed that the maximum error of the first three-order natural frequencies was within 1.03%, which verified the correctness of the analytical model. The proposed elastodynamic model included all the kinematic constraints of the manipulator without increasing the Lagrangian multiplier. The method is computationally efficient and assesses the dynamic behaviors of the mechanism at the predesign phase.

1. Introduction

Parallel manipulators (PMs) have presented great commercial value in high-speed processing and sorting due to their high stiffness, excellent dynamic performance, and reconfigurability [1]. The successful commercial parallel robots include the Delta robot [2], Tricept robot [3], Z3 robot [4], and Exechon robot [5].

The dynamic index is crucial for the performance evaluation of PMs, and excellent dynamic performance ensures stability and accuracy under the high-speed operation of PMs. An analytical elastodynamic model can identify regions in the workspace with poor dynamics, which vibrates the structure extremely. Research on the dynamic modeling of PMs has undergone a transition from rigid-body dynamics to elastic dynamics modeling. Initially, the model is established under the assumption that all components are rigid bodies [6]. Typical rigid-body dynamic models include Kane's method [7], Lagrangian formulation [8], and recursive Newton–Euler formulation [9]. The flexibility of components is considered in dynamic models to evaluate the natural frequency that represents the mechanism's ability to resist vibration. The most common elastodynamic models mainly include the finite-element method (FEM), Lagrangian formula, and substructure synthesis. Zhu et al. [10] established the 3-TPT PM's elastodynamic model using the FEM. Palmieri et al. [11] analyzed the natural frequencies of a PM through the FEM. The FEM, which can achieve higher calculation accuracy, is usually used for components with irregular sectional shapes. However, the grid needs to be remeshed for each configuration, which causes a high computational cost. Therefore, the FEM is often used to verify the theoretical model at the prototype stage.

Mathieu et al. [12] used the Lagrangian formulation to establish the elastodynamic model of the delta PM to analyze its natural frequency. Coralie et al. [13] analyzed the first 90-order natural frequencies

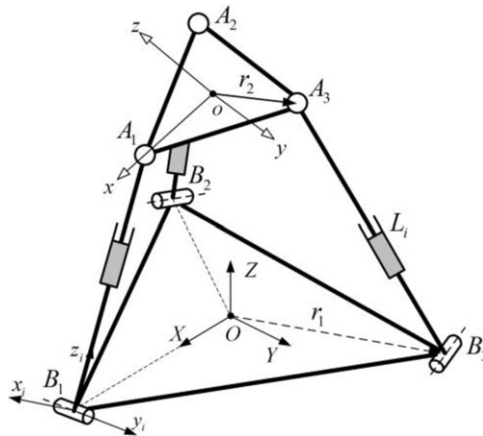


Figure 1. Schematic diagram of the 3-RPS PM.

of the planar manipulator by establishing its elastic dynamic model with the Lagrangian formulation. However, the aforementioned Lagrangian formulation requires additional Lagrangian multipliers and constraint equations, which increases the number of unknown variables and computational cost [14].

Substructure synthesis technology establishes the dynamic equation of each open-loop substructure and then assembles it into a complete dynamic model through the kinematic constraint equation. Zhang et al. [15] analyzed the natural frequency distribution in the workspace by developing an elastodynamic model of the 3-DOF 3PRS PM with substructure synthesis. Liu et al. [16] predicted the natural frequency distribution in the workspace by developing the elastodynamic model of the 8-PSS PM. Wu et al. [17] established the elastodynamic model of hybrid robots based on the substructure synthesis technology. Lian et al. [18–19] investigated the natural frequency distribution in the workspace by elastodynamic modeling in terms of the FEM and substructure synthesis technology. Shankar et al. [20] studied the first natural frequency of a 2-DOF translational parallel robot. Furthermore, Hovenars et al. [21] analyzed the natural frequency of a planar parallel robot combined with the Jacobian analysis and constraint equations. Wu et al. [22–23] proposed bond graph modeling to investigate the natural frequency of PMs.

The above mentioned method requires additional Lagrange multipliers or simultaneous kinematic constraint equations to avoid violating the kinematic constraint of the mechanism. The main contribution of the work is that the elastodynamic model is established based on the independent displacement coordinates and substructure synthesis technology. It consists of all the kinematic constraints of the manipulator and has achieved high computational efficiency without kinematic constraint equations or Lagrangian multipliers.

The remainder of the work is organized as follows. The 3-RPS PM’s structure and kinematic analysis are described in Section 2. Section 3 presents the elastodynamic modeling of the 3-RPS PM based on the substructure synthesis technology. Section 4 shows the conclusions.

2. Structure description and kinematic analysis of the 3-RPS PM

Figure 1 shows a 3-DOF 3RPS PM [24] that links the moving platform via the R-joint at point B_i to the base through the spherical joint at point A_i . Each chain consists of upper and lower links with three translational actuators. $\Delta A_1A_2A_3$ and $\Delta B_1B_2B_3$ are equilateral triangles ($oA_1 = oA_2 = oA_3 = r_2$, and $OB_1 = OB_2 = OB_3 = r_1$). The revolute joint’s axis is perpendicular to vector OB_i and in the plane $B_1B_2B_3$. The physical and geometric parameters of the manipulator are as follows: material density $\rho = 7820 \text{ kg/m}^3$; shear modulus $G = 77 \text{ GPa}$; moving platform’s thickness $h = 20 \text{ mm}$; elastic modulus $E = 200 \text{ GPa}$; link diameter $d_i = 100 \text{ mm}$; r_1 and r_2 are 0.3 and 0.2 m, respectively.

The global coordinate system, moving coordinate system, and limb coordinate system are respectively attached at the base, moving platform, and limb, for kinematic analysis (see Fig. 1). Inverse kinematics analysis of the mechanism is required to obtain the length of the connecting rod under a given end position and posture of the mechanism, which is necessary for the dynamic performance evaluation of the mechanism in the workspace.

According to the T&T angle [25], the rotation matrix from the moving system to the fixed system is defined by:

$$\mathbf{R} = \begin{bmatrix} c^2\varphi c\theta + s^2\varphi & c\varphi c\theta s\varphi - s\varphi c\varphi & c\varphi s\theta \\ c\varphi c\theta s\varphi - s\varphi c\varphi & s^2\varphi c\theta + c^2\varphi & s\varphi s\theta \\ -c\varphi s\theta & -s\varphi s\theta & c\theta \end{bmatrix} \quad (1)$$

where θ and ϕ are the orientation angles of the mechanism about the x - and y -axes, respectively.

Equation (2) shows the relation between the orientation and position coordinates of the mechanism end point:

$$\begin{cases} x = \frac{r_2 (c\theta - 1) c (2\varphi)}{2} \\ y = \frac{r_2 (1 - c\theta) s (2\varphi)}{2} \end{cases} \quad (2)$$

where x and y are the position coordinates of the point of the mechanism along the x - and y -axes, respectively.

Closed-loop vectors are used to determine the inverse kinematics of the manipulator:

$$\mathbf{B}_i \mathbf{A}_i = \mathbf{Oo} + \mathbf{Ro} \mathbf{A}_i - \mathbf{OB}_i \quad (3)$$

Thus, the actuator length of the link can be obtained as $L_i = |\mathbf{B}_i \mathbf{A}_i|$.

3. Elastodynamic model

Natural frequency, especially the fundamental frequency, is the main dynamic performance index of PMs. The higher fundamental frequency leads to higher control bandwidth and better dynamic performance. An accurate elastodynamic model should be established before exploring the 3-RPS PM's dynamic behaviors. Substructure synthesis technology is used to split the PM of a multi-closed-loop system into multiple independent open-loop substructures to establish the dynamic equations of each substructure separately. Finally, the substructures are assembled into a multi-closed-loop system through the motion constraint equation to form a complete dynamic equation of the mechanism. The substructure synthesis is adopted as the dynamic modeling method in the work. The basic analysis process can be found in ref. [15]. The assumptions are considered as follows for the dynamic modeling: the moving platform is considered as a rigid body, and other components are elastic bodies; joints are ideal constraints and perfect rigid; the system satisfies the small deformation hypothesis and instantaneous structure assumption; frictions are ignored. The work focuses on the natural frequency analysis instead of the rigid motion of the mechanism (i.e., inertial force). However, a combination with the kinematic constraint equation or the Lagrangian multiplier is required for the traditional dynamic modeling of PMs, which hinders solving the dynamic model.

The identification of independent displacement coordinates for multi-body systems has always been one of the challenges in the dynamic modeling of the PM. An identification method for independent coordinates of the multi-body PM is established based on the multipoint constraint theory, linear algebra, and singularity analysis. After that, the elastodynamic model of the PM is established by substructure synthesis technology. It has high computational efficiency because simultaneous kinematic constraint equations or increased Lagrange multipliers are not required.

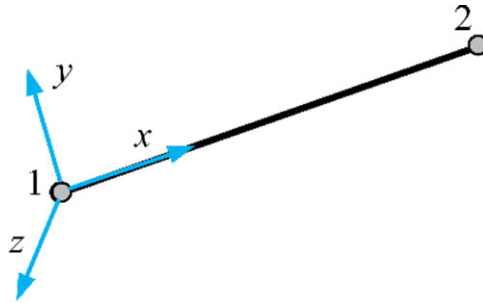


Figure 2. Spatial element beam.

3.1. Elastodynamic equation of the unconstrained substructure

Ref. [26] showed that replacing the Euler–Bernoulli beam element with the Timoshenko beam element will not significantly affect the stiffness performance of the PM. The work focuses on a dynamic modeling method that combines global-independent generalized coordinates and substructure synthesis techniques. Besides, the Euler–Bernoulli beam element is adopted to model the rod. For slender members, the Euler–Bernoulli beam can be replaced by the Timoshenko beam element. Figure 2 shows the Euler–Bernoulli beam element. When the rod is discretized into s elements, the elastodynamic equation [17] of the rod is expressed as:

$$M_e \ddot{\mathbf{u}}_i + K_e \mathbf{u}_i = \mathbf{f}_i \tag{4}$$

where $\mathbf{u}_i = [{}^i \Delta_{Bi}, {}^i \Phi_{Bi}, {}^i \mathbf{u}_{in,i}, {}^i \Delta_{Ai}, {}^i \Phi_{Ai}]^T$ and $\mathbf{f}_i = [{}^i \mathbf{f}_{Bi}^T, {}^i \mathbf{m}_{Bi}^T, {}^i \mathbf{f}_{in,i}^T, {}^i \mathbf{m}_{in,i}^T, {}^i \mathbf{f}_{Ai}^T, {}^i \mathbf{m}_{Ai}^T]^T$ are the element node coordinate vector and the external load vector of the i th rod in the coordinate system $B_i-x_i y_i z_i$, respectively; ${}^i \Delta_{Ai} ({}^i \Phi_{Ai})$ and ${}^i \Delta_{Bi} ({}^i \Phi_{Bi})$ are the linear (angular) displacement coordinates of nodes A_i and B_i in the coordinate system $B_i-x_i y_i z_i$, respectively; ${}^i \mathbf{u}_{in,i}$ is the inner nodes of the i th rod; $\mathbf{f}_{Bi}(\mathbf{m}_{Bi})$ and $\mathbf{f}_{Ai}(\mathbf{m}_{Ai})$ are the force (couple) acting on points B_i and A_i in coordinate system $B_i-x_i y_i z_i$, respectively; $\mathbf{f}_{in,i}$ and $\mathbf{m}_{in,i}$ are force and moment corresponding to the inner nodes, respectively.

The expressions of the elastodynamic equation of the rod in the global coordinate system are given as follows:

$$M_i \ddot{\mathbf{U}}_i + K_i \mathbf{U}_i = \mathbf{F}_i \tag{5}$$

where $M_i = T_i M_e T_i^T$; $K_i = T_i K_e T_i^T$; $\mathbf{F}_i = T_i \mathbf{f}_i$; $\mathbf{U}_i = T_i \mathbf{u}_i$; T_i is the transformation matrix:

$$T_i = \text{diag} \left[\underbrace{\mathbf{R}_i, \dots, \mathbf{R}_i}_{2(s+1)\mathbf{R}_i} \right] \tag{6}$$

where \mathbf{R}_i is the rotation matrix from limb (substructure) coordinate system $B_i-x_i y_i z_i$ to global coordinate system $O-XYZ$.

The elastodynamic equation for the substructure of the rigid moving platform in the global coordinate system is expressed as follows:

$$M_p \ddot{\mathbf{U}}_p = \mathbf{F}_p \tag{7}$$

where $M_p = T_p {}^o M_p T_p^T$, T_p is the transforming matrix, ${}^o M_p$ is the moving platform’s mass matrix in system $o-xyz$, $\mathbf{U}_p = [\Delta_p^T, \Phi_p^T]^T$, Φ_p and Δ_p are the global angular and linear displacement coordinates of point o , respectively, $\mathbf{F}_p = [\mathbf{f}_p^T, \mathbf{m}_p^T]^T$ is external load at point o , and \mathbf{f}_p and \mathbf{m}_p represent force and moment, respectively:

Equation (11) is transformed into the elastodynamic equation of the manipulator:

$$\overline{\mathbf{M}}\ddot{\mathbf{U}} + \overline{\mathbf{K}}\mathbf{U} = \overline{\mathbf{F}} \tag{13}$$

where $\overline{\mathbf{M}} = \sum_{i=1}^3 \overline{\mathbf{M}}_i + \overline{\mathbf{M}}_p$; $\overline{\mathbf{K}} = \sum_{i=1}^3 \overline{\mathbf{K}}_i$; $\overline{\mathbf{F}} = \sum_{i=1}^3 \overline{\mathbf{F}}_i + \overline{\mathbf{F}}_p$.

According to the kinematic constraints of the mechanism, the linear displacement coordinates Δ_{B_i} and angular displacement coordinates $\Phi_{B_{zi}}$ connected to the base are zero. They should be eliminated from the expanded displacement coordinates in Eq. (13), as well as the corresponding rows and columns of $\overline{\mathbf{M}}$ and $\overline{\mathbf{K}}$:

$$\mathbf{M}_r \ddot{\mathbf{U}}_r + \mathbf{K}_r \mathbf{U}_r = \mathbf{F}_r \tag{14}$$

where \mathbf{U}_r is the generalized displacement coordinate of the manipulator with zero displacements eliminated:

$$\mathbf{U}_r = [\phi_{B_{x1}} \quad \phi_{B_{y1}} \quad \mathbf{u}_{in,1}^T \quad \Phi_{A1}^T \quad \phi_{B_{x2}} \quad \phi_{B_{y2}} \quad \mathbf{u}_{in,2}^T \quad \Phi_{A2}^T \quad \phi_{B_{x3}} \quad \phi_{B_{y3}} \quad \mathbf{u}_{in,3}^T \quad \Phi_{A3}^T \quad \Delta_p^T \quad \Phi_p^T]^T \tag{15}$$

According to the kinematic constraint characteristic of the revolute joint, only one independent angular displacement coordinate exists. Based on the boundary conditions and multipoint constraint theory, the constraint equations of the R-joints connected to the base can be expressed as follows:

$$\begin{cases} {}^i \Delta_{B_i} = 0_{3 \times 1} \\ {}^i \phi_{B_{xi}} = {}^i \phi_{B_{zi}} = 0 \end{cases} \quad (i = 1, 2, 3) \tag{16}$$

Eq. (16) is transformed into the expression in the global coordinate system:

$$\begin{cases} \Delta_{B_i} = 0_{3 \times 1} \\ \phi_{B_{zi}} = 0 \\ \phi_{B_{xi}} = \frac{R_i(1,2)}{R_i(2,2)} \phi_{B_{yi}} \end{cases} \quad (i = 1, 2, 3) \tag{17}$$

where $R_i(j, k)$ is the j th row and the k th column of the matrix \mathbf{R}_i .

If $\Phi_{B_{xi}}$ is extracted as the independent angular displacement coordinates, the third equation of Eq. (17) can be expressed as:

$$\phi_{B_{yi}} = \frac{R_i(2, 2)}{R_i(1, 2)} \phi_{B_{xi}} \quad (i = 1, 2, 3) \tag{18}$$

The denominator of Eq. (18) is zero in some configurations, and the mapping equation determined by Eq. (18) is singular in this case. Thus, $\Phi_{B_{yi}}$ is considered an independent angular displacement coordinate of point B_i .

Accordingly, the independent generalized displacement coordinates of the mechanism are identified as follows:

$$\mathbf{U} = [\phi_{B_{y1}} \quad \mathbf{u}_{in,1}^T \quad \Phi_{A1}^T \quad \phi_{B_{y2}} \quad \mathbf{u}_{in,2}^T \quad \Phi_{A2}^T \quad \phi_{B_{y3}} \quad \mathbf{u}_{in,3}^T \quad \Phi_{A3}^T \quad \Delta_p^T \quad \Phi_p^T]^T \tag{19}$$

Therefore, the mapping relationship between \mathbf{U}_r and \mathbf{U} is defined by:

$$\mathbf{U}_r = \mathbf{Q}\mathbf{U} \tag{20}$$

$$\mathbf{Q} = \begin{bmatrix} \frac{R_1(1,2)}{R_1(2,2)} & \mathbf{0}_{1 \times (18s-1)} \\ 1 & \mathbf{0}_{1 \times (18s-1)} \\ \mathbf{0}_{(6s-6) \times 1} & \mathbf{E}_{6s-6} & \mathbf{0}_{(6s-6) \times (12s+5)} \\ \mathbf{0}_{3 \times (6s-5)} & \mathbf{E}_3 & \mathbf{0}_{3 \times (12s+2)} \\ \mathbf{0}_{1 \times (6s-2)} & \frac{R_2(1,2)}{R_2(2,2)} & \mathbf{0}_{1 \times (12s+1)} \\ \mathbf{0}_{1 \times (6s-2)} & 1 & \mathbf{0}_{1 \times (12s+1)} \\ \mathbf{0}_{(6s-6) \times (6s-1)} & \mathbf{E}_{6s-6} & \mathbf{0}_{(6s-6) \times (6s+7)} \\ \mathbf{0}_{3 \times (12s-7)} & \mathbf{E}_3 & \mathbf{0}_{3 \times (6s+4)} \\ \mathbf{0}_{1 \times (12s-4)} & \frac{R_3(1,2)}{R_3(2,2)} & \mathbf{0}_{1 \times (6s+3)} \\ \mathbf{0}_{1 \times (12s-4)} & 1 & \mathbf{0}_{1 \times (6s+3)} \\ \mathbf{0}_{(6s-6) \times (12s-3)} & \mathbf{E}_{6s-6} & \mathbf{0}_{(6s-6) \times 9} \\ \mathbf{0}_{3 \times (18s-9)} & \mathbf{E}_3 & 6 \\ \mathbf{0}_{6 \times (18s-6)} & \mathbf{E}_6 & \end{bmatrix} \tag{21}$$

Finally, the complete dynamic governing equation is obtained as follows:

$$\mathbf{M}\ddot{\mathbf{U}} + \mathbf{K}\mathbf{U} = \mathbf{F} \tag{22}$$

where $\mathbf{K} = \mathbf{Q}^T \mathbf{K}_r \mathbf{Q}$ is the overall stiffness matrix and $\mathbf{M} = \mathbf{Q}^T \mathbf{M}_r \mathbf{Q}$ is the overall mass matrix.

Ref. [15] only considers the deformation coordination between the moving platform and limbs, and the boundary conditions between limbs and the base are ignored by comparing the dynamic equation. The combination of constraint equations and Lagrangian multipliers is considered in the dynamic equation in ref. [17]. The main contribution of the work is to eliminate the constraint equation and Lagrangian multiplier from the dynamic equation, which is the essential difference from refs. [15, 17]. Meanwhile, the obtained dynamic control equation is more concise. It considers all the kinematic constraints of the mechanism, which can better simulate the constraints of the mechanism.

Manipulator’s natural frequency is calculated as follows:

$$(\mathbf{K} - \omega_i^2 \mathbf{M}) \Phi_i = \mathbf{0} \tag{23}$$

where ω_i and Φ_i are the i th order circular frequency (rad/s) and corresponding mode of the manipulator, respectively.

Hz is used to express the frequency of the manipulator in engineering [27]:

$$f_i = \frac{\omega_i}{2\pi} \tag{24}$$

where f_i is the i th order natural frequency (Hz) of the manipulator.

3.3. Natural frequency verification and distribution in the regular workspace

The MPC184 element is used to simulate the perfect rigid S- and R- joints. In this paper, two configurations are used based on whether the mechanism is circular symmetry [29] to verify the theoretical model (Case 1: $z = 4.9$ m, $\phi = 0^\circ$, and $\theta = 0^\circ$; Case 2: $z = 4.9$ m, $\phi = 10^\circ$, and $\theta = -12^\circ$). Figure 3 shows the line chart between the relative error and the number of elements s , and e_i is the relative error of the i th natural frequency between the theoretical method and the FEM. Increasing the number of elements does not significantly improve the calculation accuracy of the first-order natural frequency. Even if the rod is discretized into only one element, an acceptable calculation accuracy of 0.18% for case 1 and 0.36% for case 2 can be obtained. When the number of elements increases to three, the third-order natural frequency achieves an acceptable convergence accuracy of 1.03% for case 1 and 0.77% for case 2, and the fourth- to sixth-order natural frequencies quickly converge to 2.94, 3.41, and 3.41% for the case

Table I. Natural frequencies comparison between the FEA and analytical model of the 3-RPS PM.

Case	Method	f_1	f_2	f_3	f_4	f_5	f_6
Case 1	FEA	114.87	114.88	195.15	629.39	698.11	698.11
	Theoretical	115.02	115.02	197.16	647.89	721.92	721.92
	Error (%)	0.13	0.13	1.03	2.94	3.41	3.41
Case 2	FEA	109.12	118.20	199.12	588.36	696.39	732.01
	Theoretical	109.44	118.75	200.65	606.07	720.21	761.73
	Error (%)	0.29	0.47	0.77	3.01	3.31	3.90

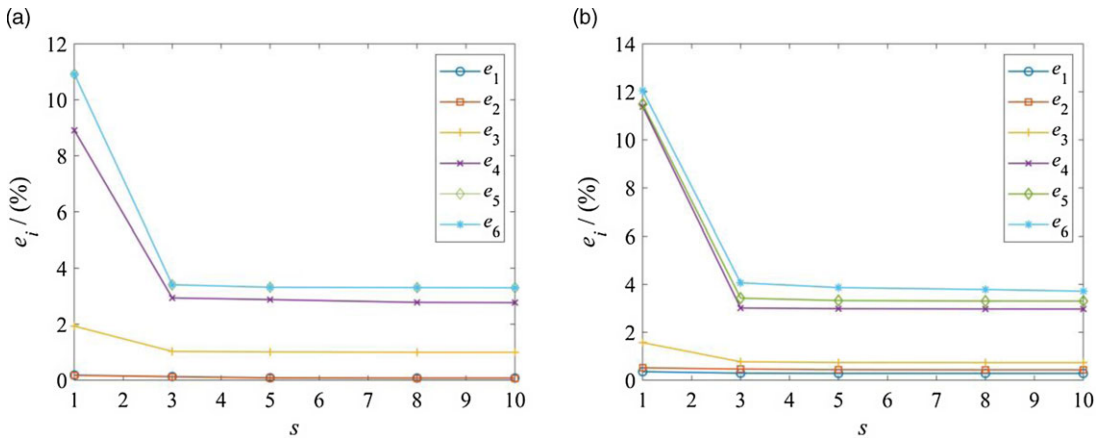


Figure 3. Line chart between relative error and the number of elements. (a) case 1 and (b) case 2.

1, 3.01, 3.31, and 3.90% for case 2, respectively. Therefore, the number of rod elements is considered as three in the work.

Table I shows that the maximum errors of the fourth-, fifth-, and sixth-order natural frequencies are 3.01, 3.41, and 3.90%, respectively. However, the maximum errors of the first three-order natural frequencies are within 1.03%. Especially, the maximum error of the first-order natural frequency is only 0.29%, which verifies the correctness of the analytical model. Figures 4–5 show the finite-element analysis results for cases 1 and 2, respectively. Compared with the computational cost of the finite-element model in 6.16 s, the theoretical model proposed in the work only takes 0.82 s, which saves 86.69% of the computational cost. Note that the moving platform shown in Figs. 4–5 is considered the elastic body with the elasticity modulus close to the rigid body to ensure the quality of the graphics. The ANSYS Workbench code is uploaded to support the correctness of the proposed theoretical model¹.

The constraints of the 3-RPS PM are considered as follows to analyze the regular workspace of the mechanism:

$$\begin{cases} L_{\min} \leq L_i \leq L_{\max} \\ |\alpha_i| \leq \alpha_{\max} \\ |\beta_i| \leq \beta_{\max} \end{cases} \quad (25)$$

where $L_{\max} = 1$ m and $L_{\min} = 0.2$ m are the upper and lower limits of the actuator, α_i and β_i the rotation angles of the spherical and revolute joints, and α_{\max} and β_{\max} is the maximum rotation angle of spherical and revolute joints.

The polar coordinate method [28] is used to obtain the regular workspace, namely the circular truncated cone composed of the largest inscribed circle in each layer of the reachable workspace. The

¹URL: <https://pan.baidu.com/s/1IzzbWlrJA56FencvObPNOg?pwd=oe93>, password: oe93.

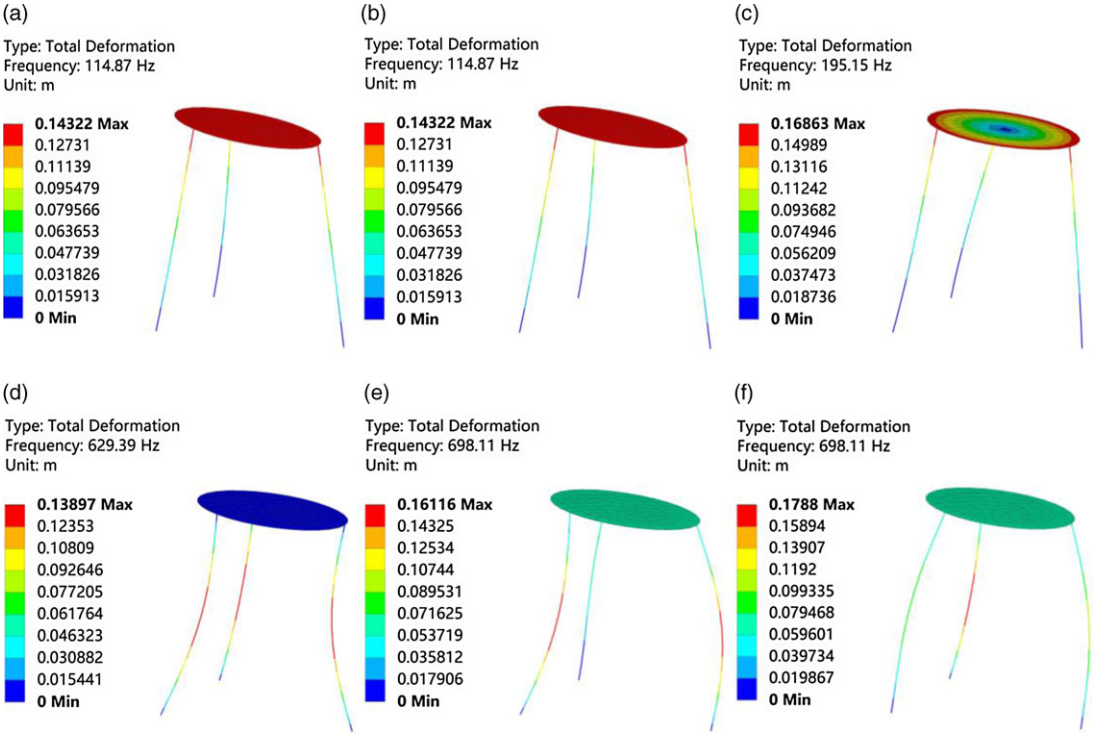


Figure 4. Finite-element analysis of case 1. (a)–(f): f_1 – f_6 .

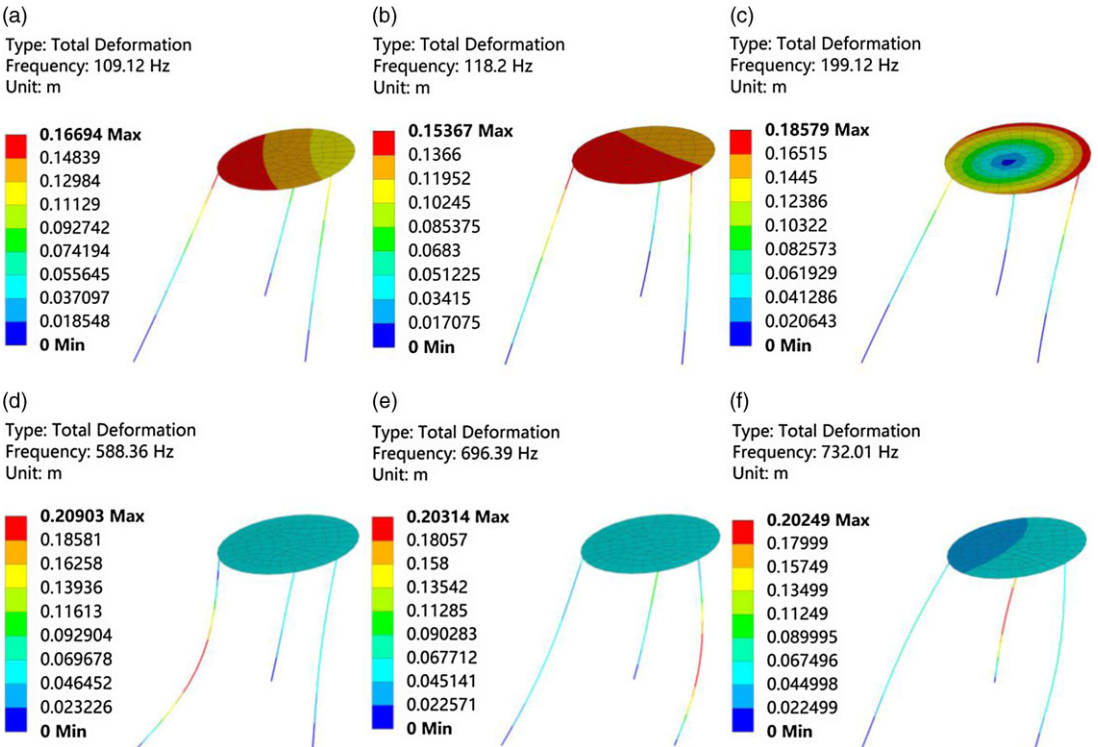


Figure 5. Finite-element analysis of case 2. (a)–(f): f_1 – f_6 .

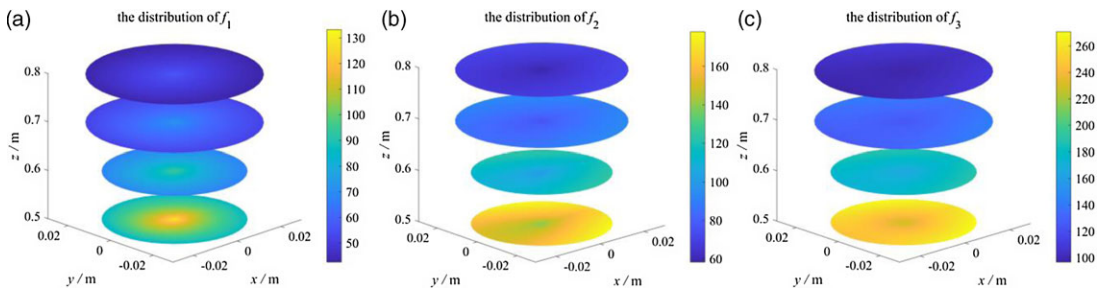


Figure 6. Distribution of the first three natural frequencies of the 3-RPS PM in the regular workspace.

distribution of natural frequencies are circularly symmetrical (Fig. 6), which is consistent with the structure of the manipulator. Besides, the increased platform height decreases the natural frequency of the mechanism. Therefore, the 3-RPS PM should work at a low height to improve its dynamic performance.

4. Conclusions

A 3-RPS PM was used as an example to propose an elastodynamic modeling and natural frequency analysis method based on the substructure synthesis method in this work. Multipoint constraint theory, linear algebra, and singularity analysis were used to identify the global independent displacement coordinates of the manipulator. After that, the elastodynamic model of the 3-PRS PM was established with substructure synthesis technology. The dynamic model including all kinematic constraints of the manipulator could achieve high solution efficiency because kinematic constraint equations or Lagrangian multipliers were not required. Compared with the FEA results, the maximum errors of the first three-order and first-order natural frequencies were less than 1.03 and 0.29%, respectively. The natural frequencies were circularly symmetric in the regular workspace and decreased with the increased platform height. The dynamic displacement response will be studied to improve the elastodynamics modeling, and some experiments will be conducted to verify the effectiveness of the proposed model in the future work.

Data availability statement. The corresponding author can provide relevant paper data.

Author contributions. GONG Yaping was responsible for the study ideas, and LOU Junbin prepared the draft.

Funding. The work was funded by the Horizontal Topic of Finite Element Analysis and Design Optimization of Key Components of Paper-Plastic Equipment (Grant No. 00520104).

Competing interests. It is confirmed that no conflict of interest exists.

References

- [1] K. Miller, "Kinematic and stiffness modeling of a novel 3-DOF RPU plus UPU plus SPU parallel manipulator," *IEEE Access* **10**, 6304–6318 (2022).
- [2] R. Clavel, "Delta, a Fast Robot with Parallel Geometry," 18th International Symposium on Industrial Robots, (1988) pp. 91–100.
- [3] B. Siciliano, "The Tricept robot: Inverse kinematics, manipulability analysis and closed-loop direct kinematics algorithm," *Robotica* **17**, 437–445 (1999).
- [4] X. Chen, X. J. Liu, F. Xie and T. Sun, "A comparison study on motion/force transmissibility of two typical 3-DOF PMs: The sprint Z3 and A3 tool heads," *Int. J. Adv. Rob. Syst.*, **11**(5), 10 (2014).
- [5] K. Nagao, N. Fujiki, H. Tanaka, A. Hayashi, H. Yamaoka and Y. Morimoto, "Machining performance of robot-type machine tool consisted of parallel and serial links based on calibration of kinematics parameters," *Int. J. Auto. Technol.-Jpn* **15**(5), 611–620 (2021).
- [6] P. D. Wu, H. G. Xiong and J. Y. Kong, "Dynamic analysis of 6-SPS PM," *Int. J. Mech. Mater. Des.* **8**(2), 121–128 (2012).

- [7] C. F. Yang and J. W. Han, "Dynamic coupling analysis of a spatial 6-DOF electro-hydraulic PM using a modal decoupling method," *Int. J. Adv. Rob. Syst.*, **10**, 104 (2013).
- [8] R. Vongvit and H. T. Zhu, "Dynamic Model of The 6-Dof PM Control Using Lagrangian Equation," International Conference on Mechatronics and Applied Mechanics (ICMAM 2011) (2011) pp. 437–440.
- [9] G. L. Chen, W. D. Yu, Q. C. Li and H. Wang, "Dynamic modeling and performance analysis of the 3-PRRU 1T2R PM without parasitic motion," *Nonlinear Dyn.* **90**(1), 339–353 (2017).
- [10] C. Zhu, J. Wang, Z. Chen and B. Liu, "Dynamic characteristic parameters identification analysis of a PM with flexible links," *J. Mech. Sci. Technol.* **28**(12), 4833–4840 (2014).
- [11] G. Palmieri, M. Martarelli, M. C. Palpacelli and L. Carbonari, "Configuration-dependent modal analysis of a Cartesian parallel kinematics manipulator: Numerical modeling and experimental validation," *Meccanica* **49**(4), 961–972 (2014).
- [12] M. Rognant, E. Courteille and P. Maurine, "A systematic procedure for the elastodynamic modeling and identification of robot manipulators," *IEEE Trans. Rob.* **26**(6), 1085–1093 (2010).
- [13] C. Germain, S. Briot, S. Caro and P. Wenger, "Natural frequency computation of parallel robots," *J. Comput. Nonlinear Dyn.* **10**(2), 021004 (2015).
- [14] A. A. Shabana, *Dynamics of Multibody Systems* (Cambridge University Press, New York, USA, 2005).
- [15] J. Zhang, Y. Q. Zhao and M. Ceccarelli, "Elastodynamic model-based vibration characteristics prediction of a three prismatic-revolute-spherical parallel kinematic machine," *J. Dyn. Syst.-Trans. ASME*, **138**(4), 041009 (2016).
- [16] Y. Zhao, F. Gao, X. Dong and X. Zhao, "Dynamics analysis and characteristics of the 8-PSS flexible redundant PM," *Rob. Comput.-Integr. Manuf.* **27**(5), 918–928 (2011).
- [17] L. Wu, G. Wang, H. Liu and T. Huang, "An approach for elastodynamic modeling of hybrid robots based on substructure synthesis technique," *Mech. Mach. Theory* **123**, 124–136 (2018).
- [18] B. Lian, X. V. Wang and L. Wang, "Static and dynamic optimization of a pose adjusting manipulator considering parameter changes during construction," *Rob. Comput.-Integr. Manuf.* **59**, 267–277 (2019).
- [19] B. Lian, L. Wang and X. V. Wang, "Elastodynamic modeling and parameter sensitivity analysis of a PM with articulated traveling plate," *Int. J. Adv. Manuf. Technol.* **102**(5-8), 1583–1599 (2019).
- [20] S. S. Ganesh and A. B. K. Rao, "Design optimization of a 2-DOF parallel kinematic machine based on natural frequency," *J. Mech. Sci. Technol.* **34**(2), 835–841 (2020).
- [21] A. G. L. Hoevenaars, S. Krut and J. L. Herder, "Jacobian-based natural frequency analysis of parallel manipulators," *Mech. Mach. Theory* **148**, 103755 (2020).
- [22] J. Wu, G. Yu, Y. Gao and L. P. Wang, "Mechatronics modeling and vibration analysis of a 2-DOF parallel manipulator in a 5-DOF hybrid machine tool," *Mech. Mach. Theory* **121**, 430–445 (2018).
- [23] J. Wu, T. M. Li and J. S. Wang, "Stiffness and natural frequency of a 3-DOF parallel manipulator with consideration of additional leg candidates," *Rob. Auto. Syst.* **61**, 868–875 (2013).
- [24] R. Desai and S. Muthuswamy, "A forward, inverse kinematics and workspace analysis of 3rps and 3rps-r parallel manipulators," *Iranian J. Sci. Technol. Trans. Mech. Eng.* doi: [10.1007/s40997-020-00346-9](https://doi.org/10.1007/s40997-020-00346-9).
- [25] I. A. Bonev, *Geometric Analysis of PMs* (Universite Laval, Canada, 2002).
- [26] C. Yang, Q. C. Li and Q. H. Chen, "Natural frequency analysis of parallel manipulators using global independent generalized displacement coordinates," *Mech. Mach. Theory* **156**, 104145 (2021).
- [27] C. Yang, W. Ye and Q. Li, "Review of the performance optimization of parallel manipulators," *Mech. Mach. Theory* **170**, 104725 (2022).
- [28] C. Yang, Q. Li and Q. Chen, "Multi-objective optimization of PMs using a game algorithm," *Appl. Math. Model* **74**, 217–243 (2019).
- [29] S. J. Yan, S. K. Ong and A. Y. C. Nee, "Stiffness analysis of parallelogram-type parallel manipulators using a strain energy method," *Rob. Cim-Int. Manuf.* **37**, 13–22 (2016).